

Preparation and study of Z-type heterojunction composite photocatalytic material with Ag₂MoO₄ modified rosette-like Bi₂WO₆ with Ag-SPR promoting effect

Yufen Gu (✉ guyf@lut.edu.cn)

Lanzhou University of Technology <https://orcid.org/0000-0003-3121-1401>

Guo Bobo

Lanzhou University of Technology

Research Article

Keywords: AMO nanoparticles, rosette-like structure BWO, Ag/AMO/BWO heterojunction, photocatalytic degradation, organic pollutants

Posted Date: March 3rd, 2021

DOI: <https://doi.org/10.21203/rs.3.rs-257054/v1>

License:   This work is licensed under a Creative Commons Attribution 4.0 International License.

[Read Full License](#)

Abstract

Here, the novel Ag₂MoO₄/Bi₂WO₆ (AMO/BWO) heterojunction composite photocatalysts were synthesized by a two-step method (co-precipitation method + hydrothermal method) and characterized by a variety of characterization techniques including XRD, XPS, SEM, TEM, UV-vis DR spectroscopy, PL spectroscopy and FTIR spectroscopy, as well as EIS analyses, and photocurrent response for confirming the formation of Z-type heterojunctions. The generation and transfer of electron/holes in the AMO/BWO heterojunctions excited by simulated sunlight were analyzed. Under simulated sunlight, the photocatalytic performance of AMO/BWO composites were studied by degradation of organic pollutants. The experimental results show that the 30wt%AMO@BWO is the best photocatalytic composite material among all samples. Due to the prolonging of lifetime of the photoexcited electrons in the CB of AMO and holes in the VB of BWO, these carriers are more effective to participate in photodegradation reactions. An electron/hole transfer mechanism of the Z-scheme heterojunctions is proposed to illustrate the enhanced photodegradation performance of the AMO/BWO composite samples.

1. Introduction

Nowadays, along with the progress of society and rise of new industries, the chemical and pharmaceutical industries are developing rapidly; simultaneously various organic pollutants and chemical dyes are discharged into the environment, such as rhodamine B (RhB), methyl orange (MO), methylene blue (MB), tetrabromobisphenol A (TBBPA), and tetracycline hydrochloride (TC). Most of the organic pollutants are toxic, carcinogenic, and chemically extremely stable. Under natural conditions, they cannot self-decompose [1], so that we must find green and environment-friendly methods to manually remove these hazardous organic pollutants. In recent years, semiconductor-based photocatalysis technology has developed rapidly, which is a new and green technology, and has been widely used in organic pollutant degradation, sterilization, and water separation [2-3]. The application of semiconductor catalytic technology has become more and more attractive in many aspects. Advanced, non-toxic, with extremely high efficiency, convenient and simple operation, no secondary pollution to the environment and lower cost [4], so it is necessary for us to design and construct Z-type, p-n type and other heterojunctions composite semiconductor photocatalytic materials with visible light response [5]. Construction of heterojunction is compared with traditional treatment methods of organic pollutants, including physical adsorption [6], chemical reaction [7] and biodegradation [8] can not only inhibit the recombination of photogenerated electrons and holes, but also broaden the absorption range of the spectrum. In the photocatalysis process, the main active species are hydroxyl radicals, superoxide radicals, and holes, which are the most important factors for the catalytic oxidation of organic pollutants [9-11].

Among semiconductors, silver-based semiconductors have good photocatalytic efficiency, which have been a hot topic in recent years. Moreover, the element silver has surface plasmon resonance, which will broaden the spectral response and further play the role in transferring photogenerated electron/hole. Among them, Ag₂MoO₄ (AMO) has a relatively low VB and CB position, suggesting that AMO can be

combined with most other semiconductor materials to build heterojunctions with special photocatalytic performances [12,13]. The nature and the strong potential to generate hydroxyl radicals and good electrical conductivity have attracted strong attention [14-16]. However, AMO is a wide band gap n-type semiconductor, which can only be excited under ultraviolet light ($\lambda < 380$ nm) [17]. The low light absorption range and poor photocatalytic performance lead to its rare application in the field of photocatalysis [18]. Like most silver-based photocatalytic materials, the surface silver ions of the AMO material will be reduced to metallic silver due to light corrosion under the sunlight [19,20].

Bismuth tungstate (Bi_2WO_6 , BWO) is also one of the most popular semiconductors in recent years. The Aurigillius-type BWO has a special crystal structure, which is a layered structure and has a suitable light absorption range. In addition, it also has a W 5d orbital guide conduction band (CB), and special valence band (VB) formed by O 2p and Bi 6s hybrid orbitals. The special layered structure and energy band structure give BWO excellent photocatalytic performance [21] for wastewater treatment and photoreduction to prepare CO_2 . However, in the process of photocatalytic degradation of pollutants, there is also a fast and easy recombination of photogenerated electron/hole, which greatly limits its photocatalytic performance. People build different heterojunctions through the load of precious metals (such as silver and silver nanowires, gold, platinum nanoparticles) and other semiconductors. For example, $\text{MoS}_2/\text{Bi}_2\text{WO}_6$, $\text{Ag}_3\text{VO}_4/\text{Bi}_2\text{WO}_6$, $\text{g-C}_3\text{N}_4/\text{Bi}_2\text{WO}_6$, $\text{Bi}_2\text{WO}_6/\text{BiOI}$, $\text{CeO}_2/\text{Bi}_2\text{WO}_6$, $\text{Bi}_2\text{WO}_6/\text{TiO}_2$, $\text{Bi}_2\text{WO}_6/\text{BiVO}_4$, and $\text{Fe}_3\text{O}_4/\text{Bi}_2\text{WO}_6$ have exactly confirmed that the construction of heterojunctions can improve the photocatalytic performance [22-26].

In this work, we adopted a two-step method – hydrothermal method + co-precipitation method – to self-assemble AMO particles onto BWO. The constructed AMO/BWO heterojunction photocatalysts have excellent performance for the separation and transfer of photogenerated holes and electrons. The photocatalytic performance of as-prepared AMO@BWO photocatalytic materials was investigated under simulated sunlight. The optimal composite sample is confirmed to be 30wt%AMO@BWO according to the photodegradation of RhB. Further, we have studied the application of the 30wt% AMO@BWO composite material in photocatalytically degrading other typical organic dyes and pollutants.

2. Experimental

2.1 Materials

All reagents used are of analytical grade and no further processing is required.

2.2 Preparation of rosette-shaped BWO

Here, the rosette-like BWO was prepared by a hydrothermal method. First, weighed out 0.9702g (0.002mol) $\text{Bi}(\text{NO}_3)_3 \cdot 5\text{H}_2\text{O}$ and dissolved it in 20mL of glacial acetic acid, and stirred it magnetically for 30 minutes until there were no suspended particles, as solution A. Then weighed out 0.3298g (0.001mol) $\text{Na}_2\text{WO}_4 \cdot 2\text{H}_2\text{O}$ and dissolved it in 20mL of deionized water, stirred it magnetically for 30 minutes until

there were no suspended particles, as solution B. The solution B was slowly added dropwise to the solution A for 30 minutes. 70 mL deionized water was added to the mixture solution, and then transferred to a 100mL polytetrafluoroethylene liner. The liner was put into the autoclave to seal; The hydrothermal reaction was carried out at 200°C for 24h in the drying box. Finally, the precipitate was collected, washed and dried to obtain the BWO sample.

2.3 Preparation of AMO@BWO composite catalyst

In a typical composite sample preparation process, 0.4 g of the prepared BWO was weighed out and dispersed in 40 mL of deionized water, which was stirred magnetically for 30 minutes. 0.1549 g of AgNO_3 was dissolved in the above solution, and then magnetically stirred for 60 minutes as Solution C. 0.1103g of $\text{Na}_2\text{MoO}_4 \cdot 2\text{H}_2\text{O}$ was dissolved in 20ml of deionized water with magnetic stirring for 30min as solution D. The solution D was slowly added to the solution C and stirred magnetically for 4 h. The whole process was carried out under shading. Finally the precipitate was collected, washed and dried to obtain composite sample 30wt%AMO@BWO. Using the same sample preparation route, 20wt% AMO/BWO and 40wt% AMO/BWO composites were also prepared with different AMO mass percentages. The schematic preparation process of the 30wt%AMO@BWO composite sample is shown in Fig. 1.

2.4 Sample characterization

Different characterization methods (X-ray powder diffraction (XRD), scanning/transmission electron microscopy (SEM/TEM), ultraviolet-visible diffuse reflectance spectroscopy (UV-vis DRS), X-ray electron energy spectroscopy (XPS), photoluminescence spectroscopy, Fourier transform infrared spectroscopy (FIR), etc.) were used to analyze the as-prepared composite materials. D8 advanced X-ray diffractometer to was used to obtain the XRD pattern of the samples to analyze the crystal structure ($\lambda_{\text{Cu-K}\alpha}=0.15406$ nm, 10° to 90° as the 2θ scanning range). UV-vis DRS spectra were measured using TU-1901 dual beam spectrophotometer. XPS measurement was carried out on PHI-5702 multifunctional X-ray photoelectron spectrometer. The transmission electron microscope and scanning electron microscope analysis of the sample were respectively used JEM-1200EX field emission transmission electron microscope and JSM-6701F field emission scanning electron microscope. Dual-spectrum infrared spectrophotometer was used to measure FIR spectra. Radio frequency RF-6000 fluorescence spectrophotometer was used to measure fluorescence spectrum (excitation wavelength 270nm). The electrochemical impedance spectroscopy (EIS) and photocurrent response were measured on the CST 350 electrochemical workstation. The working electrode preparation procedure was described in the previous publication [27]. Simulated sunlight emitted by a 300-watt xenon lamp (PLS-SXE300 BF) with a light power of 50 W was use as the light source. The parameters and measurement process were described detailedly in the literature [27].

2.5 Photodegradation performance testing

In this study, the organic pollutants MB aqueous solution ($C_{\text{MB}} = 5 \text{ mg L}^{-1}$), MO aqueous solution ($C_{\text{MO}} = 5 \text{ mg L}^{-1}$), RhB aqueous solution ($C_{\text{RhB}} = 5 \text{ mg L}^{-1}$), MB/MO/RhB mixed aqueous solution ($C_{\text{MB}}=C_{\text{MO}}=C_{\text{RhB}} =$

5 mg L⁻¹), TC aqueous solution (C_{TC} = 5 mg L⁻¹), TBBPA aqueous solution (C_{TBBPA} = 5 mg L⁻¹) were used to analyze the photocatalytic performances of the samples. 100 mL of pollutant solution and 0.03 g of catalyst were used as the photoreaction solution. Before using a 300-watt xenon lamp (PLS-SXE300 BF solar simulator) to irradiate the reaction solution to initiate photocatalysis, the photocatalyst and the photoreaction solution were adsorbed for 30 minutes in a dark environment. Then in the process of photocatalytic degradation of pollutants, a certain reaction was pipetted out and put into a 5mL centrifuge tube, and centrifuged to remove the photocatalyst in the reaction solution. UV-vis absorption spectra of the reaction solution were measured on an UV759 UV-vis spectrophotometer. According to the absorbance change at the maximum absorption wavelength, the residual concentration of the pollutant was obtained. Using the formula $\eta = (1 - C_t / C_0) \times 100\%$ (C₀ → initial pollutant concentration, C_t → residual pollutant concentration at t min) to calculate the degradation efficiency (η).

3. Results And Discussion

Fig. 2 shows the XRD patterns of as-prepared 30wt%AMO@BWO, AMO, and BWO materials, where "▽" represents the AMO in the composite sample. It can be seen that the BWO spectrum is completely matched with the standard diffraction card PDF#73-2020, and there was no impurity peak, which indicates that the BWO prepared by the experiment is the pure orthorhombic crystal structure with the unit cell parameter a = 0.5457 nm, b = 0.5436 nm and c = 1.6427 nm. In addition, all the diffraction peaks of AMO are in good agreement with the standard diffraction card PDF#08-0473 [20, 28], and no other irrelevant diffraction peaks are found. This implies the synthesis of pure cubic AMO with the unit cell parameter a = b = c = 0.9313 nm. Moreover, the diffraction peak of AMO was very narrow, indicated that the grain size of AMO is large. For the 30wt%AMO@BWO composite material, obviously AMO diffraction peaks can be observed, where 2θ = 2.05, 31.82, 33.29, 38.62, 42.19 and 47.78 correspond to the crystal planes (220), (311), (222), (400), (331) and (422), indicating that AMO and BWO co-exist in the AMO@BWO composite. The crystal structure of AMO and BWO do not change. In addition, all the diffraction peak positions of the 30wt%AMO@BWO composite material agree with the diffraction peaks of bare AMO and BWO without other impurity diffraction peaks, indicating that the AMO@BWO composite photocatalyst has been successfully prepared.

Fig. 3(a) shows the UV-vis DRS spectra of AMO, BWO, and AMO@BWO composite materials. The band gap and optical absorption properties of the samples are analyzed using ultraviolet-visible diffuse reflectance spectroscopy. The photocatalytic performance of a photocatalytic material is closely related to its absorption of light. It is clear that the bare BWO sample has an important light absorption in the wavelength range below 400nm. Whereas the bare AMO has obvious light absorption in the wavelength range above 400nm, which is significantly stronger than BWO. When AMO nanoparticles are deposited on BWO, the derived AMO@BWO heterojunction composite sample have much higher strong visible light absorption than bare BWO, indicating a synergistic effect between the two semiconductors. In addition, the degree of absorption of visible light by the samples can be also judged from their colors. The color of the 30wt% AMO@BWO composite sample is obviously darker than that of the bare BWO and AMO. It can

be seen from Fig. (c)- (e) that bare BWO and AMO have milky white and reddish colors, respectively. In contrast, the 30wt% AMO@BWO composite sample exhibits a grayer color than that of bared AMO and BWO. The differential curves of the ultraviolet-visible DR spectra are used to estimate the band gap of the samples [29]. As shown in Fig. (b), the absorption edges of AMO and BWO are 363.4 and 419.5 nm, respectively, indicating that the band gap of AMO is 3.41 eV, and the band gap of BWO is 2.96 eV, whereas the band gap of the AMO@BWO composite sample does not change significantly.

By measuring the FTIR spectroscopy of the as-prepared samples (Fig. 4), the possible presence of functional groups on their surface can be further diagnosed. The Fourier transform infrared spectrum of AMO shows obvious Mo-O tensile vibration at 830cm^{-1} , which belongs to the characteristic stretching vibration signal of cubic structure AMO [30]. In the Fourier transform infrared spectrum of BWO, one can detect Bi-O stretching vibration (830cm^{-1}), W-O stretching vibration (580cm^{-1}) and W-O-W bridge stretching vibration (732cm^{-1}), which are the characteristic absorption peaks of the well-known BWO with orthogonal structure [31,32]. For the infrared spectrum of the 30wt% AMO@BWO composite sample, there are both the characteristic absorption peaks of BWO and AMO, indicating that AMO and BWO can be well coupled. For all samples, the characteristic absorption peaks detected at 1390 , 2854 and 2919cm^{-1} belong to the antisymmetric stretching vibration of the

CO_3^{2-} group, while the absorption peaks at 1637 and 3430cm^{-1} are attributed to the hydrogen-oxygen bending vibration and hydrogen-oxygen, respectively. The absorption peaks prove that there are CO_3^{2-} groups and H_2O molecules attached to the surface of the samples [33,34].

Fig. 5 shows the XPS spectra tested on the 30wt% AMO@BWO composite sample. The C element in the full spectrum is used as a reference for the binding energy scale. Fig. (a) is a full scan XPS spectrum, which clearly shows that the composite sample contains five chemical elements, namely Bi, W, O, Mo, and Ag. From the Bi-4f XPS spectrum (Fig. (b)), it can be seen that the binding energy positions of Bi-4f_{7/2} (159.2 eV) and Bi-4f_{5/2} (164.5 eV) indicate that the Bi species exists in the Bi³⁺ oxidation state [31,35]. From the W-4f core-level XPS spectrum (Fig. (c)), it can be seen from the binding energy positions of W-4f_{7/2} (35.4 eV) and W-4f_{5/2} (37.5 eV) suggest that W⁶⁺ species exist in the BWO crystal [31]. Two characteristic peaks of 530.2 and 531.7 eV are detected on the O-1s core level XPS spectrum (Fig. (d)), which correspond to lattice oxygen and chemisorption oxygen, respectively [29,35,36]. The XPS spectrum of Mo-3d core energy level (Fig. (e)) shows two peaks at 231.8 and 235.0 eV, which coincide with the binding energy of Mo⁶⁺-3d_{5/2} and Mo⁶⁺-3d_{3/2}, respectively [37]. Fig. (f) is the Ag-3d core-level XPS spectrum. The two main peaks of 367.4 (Ag⁺-3d_{5/2}) and 373.4 eV (Ag⁺-3d_{3/2}) match with the lattice Ag⁺ of AMO. The two weak peaks at 368.3 (Ag⁰-3d_{5/2}) and 374.3 eV (Ag⁰-3d_{3/2}) correspond to the metallic silver species [38] generated during the preparation of composite samples.

SEM images were measured to analyze the morphology of BWO, AMO and 30wt% AMO@BWO. As seen from Fig. 6(a), AMO exists in the form of ellipsoidal or spherical particles in the range of 1.8 to 3.8 μm. The SEM image of BWO (Fig. 6(a)) shows that the BWO crystals are self-assembled into rosette-like

hierarchical structure with size of 3-9 μ m. The hierarchical structure is assembled from nanosheets with a diameter of 300-2200nm and a thickness of 20-40nm. For 30wt% AMO@BWO composite sample, the AMO particles are self-assembled on the petals of the BWO rosette flower, and the particle size of the AMO is reduced to 30 to 70nm. The reason for this phenomenon may be that the silver ions are pre-adsorbed on the petals of BWO, and the growth of AMO is greatly restricted [39]; Furthermore, the hierarchical structure of BWO could affect the surface energy of AMO crystals and restrict their growth. The TEM image suggests a good contact between AMO with BWO, thus establishing a stable photo-generated hole and electron transfer path between them and promoting effective separation and transfer of carriers. In addition, the composite material compounded with rosette-like BWO has a larger specific surface area and provides more active sites for the photodegradation reactions of pollutants.

The microstructure of 30wt%AMO@BWO was further analyzed by TEM images to reveal the formation of heterojunctions established between AMO and BWO. It can be clearly seen from Fig. (a) and (b) that the AMO particles are well self-assembled and fixed on the petals of the rosette-like BWO. On the surface of the composite material, metal silver nanoparticles of smaller size can be also seen. This may be due to the reduction of a few silver ions into silver nanoparticles during the sample preparation process. High-resolution TEM (HR-TEM) image can further prove the formation of Ag/AMO/BWO heterojunctions, as shown in Fig. 7(c). In the HR-TEM image, AMO and BWO crystals and Ag nanoparticles can be identified by the characteristics of their lattice fringes. Fig. 7(k) shows the selected area electron diffraction (SAED) pattern, on which the polycrystalline diffraction rings clearly appear. Referring to the standard diffraction data of PDF#08-0473 (AMO cubic phase), PDF#73-2020 (BWO orthogonal phase) and PDF#87-0598 (Ag orthorhombic phase), polycrystalline diffraction rings can be well indicated. From the perspective of chemical elements, energy dispersive x-ray spectroscopy (EDS) can support the formation of heterojunctions between AMO and BWO, as shown in Fig. 7(d). In addition to the Cu/C signals of the TEM micro-mesh support [40], the chemical elements Bi/W/Ag/Mo/O are also clearly detected on the EDS spectrum. The EDS element mapping images obtained from the dark field scanning TEM (DF-STEM) image area are shown in Fig. 7 (e)-(j). The elements are uniformly distributed on the composite material, indicating a uniform coupling between the AMO particles and the BWO layered architecture.

The recombination behavior of hole-electron pairs in semiconductors can be predicted by PL fluorescence spectra, photocurrent response spectra and EIS spectra. Fig. 8 shows the fluorescence spectra of bare BWO and AMO@BWO composite samples (excitation wavelength: 270nm). It is noted that when electron-hole pairs recombine, a certain fluorescence intensity will be produced. The stronger the fluorescence intensity of the sample is, the higher the recombination efficiency of electron-hole pairs [20]. In short, the stronger fluorescence intensity implies lower photocatalytic performance of the sample [41,42]. It can be observed from the fluorescence spectra that the PL emission peaks of BWO and its derivative composite samples are between 400nm-450nm [43]. However, the fluorescence intensity of the AMO@BWO composite samples is significantly lower than that of the bare BWO sample. The loaded AMO nanoparticles can effectively promote the separation and transfer of hole-electron pairs, which is conducive to improving the photocatalytic performance of the composite samples.

Fig. 9(a) shows the photocurrent response spectra of AMO, BWO and 30wt%AMO@BWO. Under simulated sunlight irradiation with a gap of 20s (10s of light and 10s of darkness), all samples show obvious transient photocurrent response behavior. The order of photocurrent is AMO <BWO <30wt% AMO/BWO.

Fig. 9(b) depicts the EIS spectra (Nyquist format) of the samples. It can be seen that compared with bare BWO and AMO, the 30wt% AMO/BWO composite has an EIS spectrum with a smaller semicircular diameter in the high frequency region. The semicircle diameter of the EIS is usually used as an indicator of the charge transfer resistance at the electrode/electrolyte interface [44]. The EIS spectrum shows that the charge transfer resistance of the 30wt% AMO/BWO composite is small. PL spectra, photocurrent response spectra and EIS spectra can jointly indicate that the 30wt% AMO/BWO composite sample exhibits a more effective separation and transfer of photogenerated electron-hole pairs compared with bare BWO.

The photocatalytic degradation performances of AMO, BWO, and AMO@BWO composites were compared by degrading RhB ($C_{\text{RhB}} = 5\text{mg L}^{-1}$, $C_{\text{photocatalyst}} = 0.3\text{g L}^{-1}$). Fig. 10(a)-(e) display the UV-visible absorption spectra of RhB solutions photodegraded by AMO, BWO, 20wt%AMO@BWO, 30wt%AMO@BWO, and 40wt%AMO@BWO within 60 min, respectively. During the photodegradation process, the determination of the residual concentration of RhB is based on the absorbance of RhB at its maximum absorption wavelength ($\sim 554\text{ nm}$). Fig. 10(f) shows the photodegradation curves of RhB over different catalysts. It can be clearly seen that the photocatalytic performance of the AMO/BWO composites is much better than that of bare AMO and BWO. This specific phenomenon indicates that the heterojunctions are formed in the AMO/BWO composite materials, which is conducive to improving the separation efficiency of photogenerated electron-hole pairs, and synergistically enhancing the photocatalytic performance of the materials.

Among the samples, the 30wt% AMO/BWO composite shows the highest photocatalytic degradation performance. RhB is almost completely degraded within 60 min, and the degradation rate is as high as 98.6%, which is far higher than that of bared AMO ($\eta=29.5\%$ within 60 min) and BWO ($\eta=39.6\%$ within 60 min). An important parameter to quantitatively compare the photodegradation performance of photocatalysts is the reaction rate constant [45]. Fig. 10(g) depicts the $\ln(C_t/C_0) \sim t$ curves, from which it can be seen that the photodegradation process of RhB completely follows the pseudo first-order kinetics, expressed by $\ln(C_t/C_0) = -k_{\text{app}}t$ [44,46]. By comparing the apparent first-order reaction rate constants (k_{app}) between samples, the photodegradation performance of the best composite sample 30wt% AMO/BWO ($k_{\text{app}} = 0.06186\text{min}^{-1}$) is estimated to be approximately 10.47 times higher than that of bare AMO ($k_{\text{app}} = 0.00591\text{min}^{-1}$) and 7.44 times higher than that of bare BWO ($k_{\text{app}} = 0.00831\text{min}^{-1}$).

In order to apply the most ideal 30wt% AMO/BWO photocatalytic material to environmental purification in real life, we further evaluate its photodegradation performance by degrading MB, MO, RhB/MO/MB mixture, TC and TBBPA solutions. The concentration of MO, RhB and MB in the mixed solution can be estimated based on the absorbance at the maximum absorption wavelength of the dyes $\lambda_{\text{MO}} = 464\text{nm}$,

$\lambda_{\text{RhB}} = 554\text{nm}$ and $\lambda_{\text{MB}} = 663\text{nm}$. Fig. 11 (a) and (b) show the ultraviolet-visible absorption spectra of MB and MO, respectively. According to the ultraviolet-visible absorption spectra, the photodegradation curves of MB and MO can be obtained, as shown in Fig. 11(c) and (d), respectively. It is seen that the degradation rate of MB solution can reach 95.3% in 7.5 minutes, and the degradation rate of MO solution can reach 89.2% in 120 minutes. Under the action of the photocatalyst, MB and MO are basically removed.

Fig. 11 (e) and (f) display the UV-Vis absorption spectra of the RhB/MO/MB mixed solution ($C_{\text{MO}} = C_{\text{RhB}} = C_{\text{MB}} = 5 \text{ mg L}^{-1}$, $C_{\text{photocatalyst}} = 0.3 \text{ g L}^{-1}$) and the photodegradation curves of RhB, MO and MB. Interestingly, in the photodegradation progress of the mixed dyes, it can be found that MB and MO are degraded preferentially than RhB, and within 50 minutes, the degradation rates of MB and MO reach 95.5% and 80.4%, respectively. When the irradiation time exceeds 100 min, the C_t/C_0 ratios of MB and MO remain basically stable. In contrast, the photodegradation of RhB is relatively slow, basically meeting with the quasi-first-order kinetic process. Possibly the ionization of the dye, the molecular structure of the dye, the catalyst's promotion of the decomposition of the dye, the synergistic photosensitivity effect between different dyes and the adsorption characteristics of the catalyst to different dyes collectively result in the competitive photodegradation of dyes in the mixed solution.

Fig. 12 (a) and (b) show the UV-Vis absorption spectra of TC and TBBPA solutions photocatalyzed by 30wt% AMO/BWO composite photocatalyst. The concentrations of TC and TBBPA are usually characterized by the absorption peaks at 360 and 310 nm, respectively [47-49]. By comparing the relative intensities of the absorption peaks of TC and TBBPA, their photodegradation curves versus time were obtained, as given in Fig. 12(c) and (d). The corresponding pseudo first-order kinetic curves of the degradation of TC and TBBPA are inserted in in Fig. 12(c) and (d), respectively. It can be clearly seen that under the action of 30wt% AMO/BWO composite photocatalyst, TC and TBBPA are obviously degraded. When the photocatalysis progresses to 30 min, the degradation rate reach 82.5% for TBBPA ($k_{\text{app}} = 0.03585\text{min}^{-1}$). For the degradation of TC aqueous solution, under 30 min of irradiation, its degradation efficiency also reaches a relatively satisfactory value 62.9% ($k_{\text{app}} = 0.01824\text{min}^{-1}$). The above photocatalytic degradation experiments show that the 30wt% AMO/BWO composite photocatalyst has an industrial application prospect in removing various environmental pollutants.

Reactive species play a decisive role in the photocatalytic degradation process. In a typical photocatalytic degradation process, we conducted free radical capture experiments. The scavengers ethylenediaminetetraacetic acid (EDTA), benzoquinone (BQ) and isopropanol (IPA) were added to the photoreaction system ($C_{\text{RhB}} = 5\text{mg L}^{-1}$, $C_{\text{photocatalyst}} = 3\text{mg L}^{-1}$) to examine h^+ , superoxide ($\cdot\text{O}_2^-$) and hydroxyl ($\cdot\text{OH}$), respectively. The concentration of all scavengers is 1 mmol L^{-1} . In the experiment of capturing active species of $\cdot\text{O}_2^-$ radicals, the color of the reaction system changes abnormally under simulated sunlight. The reason for this phenomenon may be due to the light-induced reaction between BQ and RhB, which is proved by adding BQ in the RhB solution without photocatalyst, as shown in Fig. 13(e). It is seen that the maximum absorption peak of RhB (554nm) can still be used for the

determination of the concentration of RhB, because it is not significantly affected by the light-induced reaction between BQ and RhB. Fig. 13(f) shows the degradation curves of RhB without and with adding the three scavengers, which are derived from the UV-Vis absorption spectra shown in Fig. 13(a)-(d). Obviously, the scavengers IPA and EDTA have a significant inhibitory effect on the degradation of RhB, indicating that the degradation of RhB is closely related to the $\cdot\text{OH}$ and h^+ active species, while $\cdot\text{O}_2^-$ radicals play a secondary role.

According to the Mott-Schottky diagrams measured in Fig. 14(a) (BWO) and (b) (AMO), the Mott-Schottky method [50,51] can be used to estimate their CB potentials, which are derived to be -0.47 and +0.4eV vs standard calomel electrode (SCE), respectively. Based on the relationship between SCE and normal hydrogen electrode (NHE): $V_{\text{NHE}} = V_{\text{SCE}} + 0.059 \times \text{pH} (=7) + 0.242$ [51], and considered the bandgap of AMO (3.41 eV) and BWO (2.96 eV), the CB/VB potentials are estimated to be +1.05/+4.46 V vs NHE for AMO and +0.19/+3.15 V vs NHE for BWO. Analysis of the Mott-Schottky curves also shows that both BWO and AMO behave as n-type semiconductors.

The AMO particles are self-assembled to the hierarchical structure of rosette-like BWO, and the band structures of AMO and BWO are interlaced with each other to form the Z-scheme AMO/BWO heterojunctions, as shown in Fig. 15. Since the Fermi level of the n-type semiconductor BWO is lower than that of the n-type semiconductor AMO, electrons will spontaneously diffuse from AMO to BWO; at the same time, this electron diffusion process will generate a built-in electric field at the interface between AMO and BWO. The direction of the built-in electric field is from BWO to AMO. The built-in electric field formed will prevent the continuous diffusion of electrons, finally reaching a thermal equilibrium state at the AMO/BWO heterojunctions. However, during the photocatalytic degradation process, the thermal equilibrium state at AMO/BWO will be broken. This is due to the continuous generation of non-equilibrium holes and electrons on BWO and AMO, as shown in Fig. 15(b). The built-in electric field established at the AMO/BWO heterojunction will drive the unbalanced electrons generated in the CB of the AMO semiconductor to move to the VB of the BWO semiconductor, and finally recombine with the unbalanced holes generated in the VB of the BWO semiconductor. This electron transfer method and path greatly improves the photodegradation efficiency of the catalyst, due to the prolonged lifetime of the photogenerated electrons in the CB of AMO and holes in the VB of BWO. This enables the photogenerated holes and electrons to participate in the photodegradation reaction more effectively, which is the main mechanism for the enhanced photocatalytic performance of the AMO/BWO composites. However, it is worth noting that in the analysis of XPS and TEM, metallic silver particles exist in the AMO/BWO composite materials which act as a bridge for electron transfer between BWO and AMO and promote the movement of electrons from AMO to BWO, as shown in Fig. 15(c). The sufficiently positive VB potential of BWO (+3.15 V vs) means that the photogenerated VB holes in BWO can react with H_2O or OH^- to generate $\cdot\text{OH}$ ($\text{H}_2\text{O}/\cdot\text{OH}$) = +2.38V vs NEH, $\text{E}^0(\text{OH}^-/\cdot\text{OH}) = +1.99\text{V}$ vs NHE) [52]. Moreover, according to the active species capture experiment, $\cdot\text{OH}$ radicals play an critical role in the degradation process. In addition, $\cdot\text{OH}$ radicals are not completely derived from hole reactions, the potential of sufficiently positive photo-

generated holes in the VB of AMO (+4.46V vs NHE) indicates that $\cdot\text{OH}$ radicals may be generated through their coupling with OH^-

or H_2O species [53]. Holes have also been identified as an important active species in the photocatalysis. The generation of $\cdot\text{O}_2^-$ may come from the combination of the adsorbed O_2 with the light-excited electrons in higher exciting states of BWO. However, it is worth noting that the photogenerated electrons in the CB of BWO cannot react with O_2 to generate $\cdot\text{O}_2^-$, because the CB potential of BWO (+0.19eV vs NHE) is not negative with reference to $\text{O}_2/\cdot\text{O}_2^-$ (-0.13eV vs NHE) [54].

4. Conclusions

In this work, AMO nanoparticles were self-assembled on the surface of rosette-like BWO by a co-precipitation method to prepare a new type of AMO/BWO composite photocatalysts with Z-scheme heterojunctions, which have excellent photocatalytic performance. The AMO/BWO composite photocatalysts were used to photocatalytically degrade a variety of dyes and organic pollutants. The experimental results show that the 30wt% AMO@BWO composite sample has a photocatalytic degradation rate of 98.6% for RhB. The 30wt%AMO/BWO has the best photoexcited hole/electron pair separation and transfer efficiency, and the highest photocatalytic activity, which is 3.35 and 2.49 times higher than that of bared AMO and BWO, respectively. Based on the cross-band structure between AMO and BWO, a Z-scheme electron transfer mechanism is proposed to explain the effective carrier separation and the improvement of photocatalytic performance of the AMO/BWO heterojunction photocatalysts.

References

1. Brown, Mark A., and S. C. De Vito. "Predicting azo dye toxicity." *C R C Critical Reviews in Environmental Control* 23.3(1993):249-324.
2. Yang, Jingjing, et al. "Photocatalytic Performance and Degradation Pathway of Rhodamine B with TS-1/C3N4 Composite under Visible Light." *Nanomaterials* 10.4(2020):756.
3. Sboui, Mouheb, et al. "Paper Functionalized with Nanostructured TiO_2/AgBr : Photocatalytic Degradation of 2-Propanol under Solar Light Irradiation and Antibacterial Activity." *Nanomaterials* 10.3(2020):470.
4. Silvestri, Siara, J. F. De Oliveira, and E. L. Foletto. "Degradation of methylene blue using Zn_2SnO_4 catalysts prepared with pore-forming agents." *Materials Research Bulletin* 117.SEP. (2019):56-62.
5. Duan, Qianqian, et al. "Design of hole-transport-material free $\text{CH}_3\text{NH}_3\text{PbI}_3/\text{CsSnI}_3$ all-perovskite heterojunction efficient solar cells by device simulation." *Solar Energy* 201(2020):555-560.
6. Sharma, A.K. Singh, V.K. Shahi, *ACS Sustain. Chem. Eng.* 7, 1427–1436 (2018).
7. Yang, Z. Zeng, C. Zhang, D. Huang, G. Zeng, R. Xiao, C. Lai, C. Zhou, H. Guo, W. Xue, M. Cheng, W. Wang, J. Wang, *Chem. Eng. J.* 349, 808–821 (2018).
8. Raheem, P. Prinsen, A.K. Vuppaladadiyam, M. Zhao, R. Luque, *J. Clean. Prod.* 181, 42–59 (2018).

9. Liu, J. Shen, X. Yang, T. Zhang, H. Tang, 3D reduced graphene oxide aerogel-mediated Z-scheme photocatalytic system for highly efficient solar-driven water oxidation and removal of antibiotics. *Appl. Catal. B: Environ.* 232 (2018) 562-573.
10. Yu, X. Zhang, G. Li, Y. Cao, Y. Shao, D. Li, Highly efficient Bi₂O₂CO₃/BiOCl photocatalyst based on heterojunction with enhanced dye-sensitization under visible light, *Appl. Catal. B: Environ.* 187 (2016) 301–309.
11. Yu, G. Li, S. Kumar, K. Yang, R. Jin, Phase transformation synthesis of novel Ag₂O/Ag₂CO₃ heterostructures with high visible light efficiency in photocatalytic degradation of pollutants, *Adv. Mater.* 26 (2014) 892–898.
12. H. Xu, J. Zhang, X.Z. Lv, T.J. Niu, Y.X. Zeng, J.Z. Duan, B.R. Hou, The effective photocatalysis and antibacterial properties of AgBr/Ag₂MoO₄@ZnO composites under visible light irradiation, *Biofouling* 35 (2019) 719–731.
13. T. Liu, W.J. Li, H.D. Li, C.J. Ren, X.Y. Li, Y.J. Zhao, Efficient Fe₃O₄-C₃N₄-Ag₂MoO₄ ternary photocatalyst: synthesis, outstanding light harvesting, and superior hydroxyl radical productivity for boosted photocatalytic performance, *Appl. Catal. A-Gen.* 568 (2018) 54–63.
14. Zheng, F. Chang, M. Jiao, Q. Xu, B. Deng, X. Hu, A visible-light-driven heterojunctioned composite WO₃/Bi₁₂O₁₇Cl₂: Synthesis, characterization, and improved photocatalytic performance. *J. Colloid Interf. Sci.* 510 (2018) 20-31.
15. Zhao, Y. Liu, Z. Wei, S. Yang, H. He, C. Sun, Fabrication of a novel p-n heterojunction photocatalyst n-BiVO₄@p-MoS₂ with core-shell structure and its excellent visible-light photocatalytic reduction and oxidation activities, *Appl. Catal. B: Environ.* 185 (2016) 242-252.
16. Liu, V. Häublein, X. Zhou, U. Venkatesan, M. Hartmann, M. Mačković, P. Schmuki, "Black" TiO₂ nanotubes formed by high-energy proton implantation show noble-metal-co-catalyst free photocatalytic H₂-evolution, *Nano Lett.* 15 (2015) 6815-6820.
17. Diak, E. Grabowska, A. Zaleska, Synthesis, characterization and photocatalytic activity of noble metal-modified TiO₂ nanosheets with exposed {0 0 1} facets, *Appl. Surf. Sci.* 347 (2015) 275-285.
18. Jin, Q. Liang, Y. Song, S. Xu, Z. Li, C. Yao, *J. Alloys Compd.* 726, 221–229 (2017).
19. Li, X. Chen, Z.-L. Xue, *Sci. China Chem.* 56, 443–450 (2013).
20. Chen, X. Xie, Y. Si, P. Wang, Q. Yan, *Appl. Surf. Sci.* 498, 143860 (2019).
21. Phuruangrat, Anukorn, et al. "Hydrothermal synthesis and characterization of visible-light-driven Cl-doped Bi₂WO₆ nanoplate photocatalyst." *Journal- Ceramic Society Japan* 125.6(2017):500-503.
22. Shirzad-Siboni, Mehdi, et al. "Enhancement of photocatalytic activity of Cu-doped ZnO nanorods for the degradation of an insecticide: Kinetics and reaction pathways." *Journal of Environmental Management* 186.pt.1(2017):1-11.
23. Kenneth, et al. "Physisorption Hysteresis Loops and the Characterization of Nanoporous Materials." *Adsorption Science & Technology* 22.10(2004):773-782.

24. Tayyebi, et al. "Improved photocatalytic and photoelectrochemical performance of monoclinic bismuth vanadate by surface defect states ($\text{Bi}_{1-x}\text{VO}_4$)." *Journal of colloid and interface science* 514(2018):565-575.
25. Tiwari, Alka, et al. "Nanocomposite thin films $\text{Ag}_0(\text{NP})/\text{TiO}_2$ in the efficient removal of micro-pollutants from aqueous solutions: A case study of tetracycline and sulfamethoxazole removal." *Journal of Environmental Management* 220.AUG.15(2018):96-108.
26. Xie, Ruyi, et al. "Construction of $\text{CQDs-Bi}_{20}\text{TiO}_{32}/\text{PAN}$ electrospun fiber membranes and their photocatalytic activity for isoproturon degradation under visible light." *Materials Research Bulletin* 94.oct.(2017):7-14.
27. Tingting Cheng, Xiaofeng Sun, Tao Xian, Zao Yi, Ruishan Li, Xiangxian Wang, and Hua Yang, "Tert-butylamine/oleic acid-assisted morphology tailoring of hierarchical $\text{Bi}_4\text{Ti}_3\text{O}_{12}$ architectures and their application for photodegradation of simulated dye wastewater" *Optical Materials* 112 (2021) 110781.
28. Abulizi, K. Kadeer, L. Zhou, Y. Tursun, T. Dilinuer, J. Taiwan Inst. Chem. Eng. 88, 243–251 (2018).
29. X. Zhao, H. Yang, S.H. Li, Z.M. Cui, C.R. Zhang, Synthesis and theoretical study of large-sized $\text{Bi}_4\text{Ti}_3\text{O}_{12}$ square nanosheets with high photocatalytic activity, *Mater. Res. Bull.* 107 (2018) 180–188.
30. Ghobadifard, S. Mohebbi, P.V. Radovanovic, Selective oxidation of alcohols by using $\text{CoFe}_2\text{O}_4/\text{Ag}_2\text{MoO}_4$ as a visible-light-driven heterogeneous photocatalyst, *New J. Chem.* 44 (2020) 2858–2867.
31. Yanping Wang, Xiaofeng Sun, Tao Xian, Guorong Liu, and Hua Yang, "Photocatalytic purification of simulated dye wastewater in different pH environments by using $\text{BaTiO}_3/\text{Bi}_2\text{WO}_6$ heterojunction photocatalysts" *Optical Materials*
32. Y. Dong, X.H. Ding, T. Guo, X.P. Yue, X. Han, J.H. Sun, Self-assembled hollow sphere shaped $\text{Bi}_2\text{WO}_6/\text{RGO}$ composites for efficient sunlight-driven photocatalytic degradation of organic pollutants, *Chem. Eng. J.* 316 (2017) 778–789.
33. T. Guan, H. Yang, X.F. Sun, T. Xian, Preparation and promising application of novel $\text{LaFeO}_3/\text{BiOBr}$ heterojunction photocatalysts for photocatalytic and photo-Fenton removal of dyes, *Opt. Mater.* 100 (2020) 109644.
34. Yuxiang Yan, Hua Yang, Zao Yi, Ruishan Li, and Tao Xian, "Design of ternary $\text{CaTiO}_3/\text{g-C}_3\text{N}_4/\text{AgBr}$ Z-scheme heterostructured photocatalysts and their application for dye photodegradation" *Solid State Sciences* 100 (2020) 106102.
35. Golkari, H. Shokrollahi, H. Yang, the influence of Eu cations on improving the magnetic properties and promoting the Ce solubility in the Eu, Ce-substituted garnet synthesized by the solid state route, *Ceram. Int.* 46 (2020) 8553–8560.
36. R. Khalifeh, H. Shokrollahi, S.M. Arab, H. Yang, The role of Dy incorporation in the magnetic behavior and structural characterization of synthetic Ce, Bi-substituted yttrium iron garnet, *Mater. Chem. Phys.* 247 (2020) 122838.

37. Vosoughi, A. Habibi-Yangjeh, S. Asadzadeh-Khaneghah, S. Ghosh, T. Maiyalagan, Novel ternary g-C₃N₄ nanosheet/Ag₂MoO₄/AgI photocatalysts: Impressive photocatalysts for removal of various contaminants, *J. Photochem. Photobiol. A* 403 (2020) 112871.
38. P. Wang, H. Yang, X.F. Sun, H.M. Zhang, T. Xian, Preparation and photocatalytic application of ternary n-BaTiO₃/Ag/p-AgBr heterostructured photocatalysts for dye degradation, *Mater. Res. Bull.* 124 (2020) 110754.
39. Shi, F. Guo, S. Yuan, *Appl. Catal. B* 209, 720–728 (2017).
40. Yongchun Ye, Hua Yang, Haimin Zhang, and Jinling Jiang, “A promising Ag₂CrO₄/LaFeO₃ heterojunction photocatalyst applied to photo-Fenton degradation of RhB” *Environmental Technology* 41 (2020) 1486–
41. Das, D. Majhi, Y.P. Bhoi, B.G. Mishra, Combustion synthesis, characterization and photocatalytic application of CuS/Bi₄Ti₃O₁₂ p-n heterojunction materials towards efficient degradation of 2-methyl-4-chlorophenoxyacetic acid herbicide under visible light, *Chem. Eng. J.* 362 (2019) 588–599.
42. Y. Xu, Y.Y. Chen, X. Xie, K. Yan, Y.S. Si, M.H. Zhang, Q.S. Yan, Construction of Ag SPR-promoted Z-scheme Ag₂MoO₄/CuBi₂O₄ composites with enhanced photocatalytic performance, *J. Mater. Sci.-Mater. Electron.* 31 (2020) 8151–8164.
43. Y. Wang, S.X. Liu, W. Mao, Y.C. Bai, K. Chiang, K. Shah, J. Paz-Ferreiro, Novel Bi₂WO₆ loaded N-biochar composites with enhanced photocatalytic degradation of rhodamine B and Cr (VI), *J. Hazard. Mater.* 389 (2020) 121827.
44. Yuxiang Yan, Hua Yang, Xinxin Zhao, Ruishan Li, and Xiangxian Wang, “Enhanced photocatalytic activity of surface disorder-engineered CaTiO₃” *Materials Research Bulletin* 105 (2018) 286–290.
45. Tao Xian, Xiaofeng Sun, Lijing Di, Hongqin Li, Hua Yang, “Improved photocatalytic degradation and reduction performance of Bi₂O₃ by the decoration of Au Pt alloy nanoparticles” *Optical Materials* 111 (2021) 110614.
46. Guan S, Yang H, Sun X, et al. Preparation and promising application of novel LaFeO₃/BiOBr heterojunction photocatalysts for photocatalytic and photo-Fenton removal of dyes[J]. *Optical Materials*, 2020, 100(Feb.):109644.1-109644.11.
47. Qin, Y. Guo, D. Zhou, Y. Yang, Y. Guo, Facile growth and composition-dependent photocatalytic activity of flowerlike BiOCl_{1-x}Br_x hierarchical microspheres, *Appl. Surf. Sci.* 390 (2016) 765–777.
48. O. Oseghe, A.E. Ofomaja, Study on light emission diode/carbon modified TiO₂ system for tetracycline hydrochloride degradation, *J. Photochem. Photobiol. A* 360 (2018) 242–248.
49. Yusoff, S.A. Ong, L.N. Ho, Y.S. Wong, W. Khalik, Degradation of phenol through solar-photocatalytic treatment by zinc oxide in aqueous solution, *Desalin. Water Treat.* 54 (2015) 1621–1628.
50. Cardon, W.P. Gomes, On the determination of the flat-band potential of a semiconductor in contact with a metal or an electrolyte from the Mott-Schottky plot, *J. Phys. D Appl. Phys.* 11 (1978) L63–L67.
51. Y. Wang, H. Yang, Z. Yi, X.X. Wang, Enhanced photocatalytic performance by hybridization of Bi₂WO₆ nanoparticles with honeycomb-like porous carbon skeleton, *J. Environ. Manage.* 248 (2019) 109341.

52. Yuxiang Yan, Hua Yang, Zao Yi, Tao Xian, Ruishan Li, and Xiangxian Wang, "Construction of $\text{Ag}_2\text{S}@\text{CaTiO}_3$ heterojunction photocatalysts for enhanced photocatalytic degradation of dyes" *Desalination and Water Treatment* 170 (2019) 349–360.
53. J. Gao, F. Wang, S.F. Wang, X.X. Wang, Z. Yi, H. Yang, Photocatalytic activity tuning in a novel $\text{Ag}_2\text{S}/\text{CQDs}/\text{CuBi}_2\text{O}_4$ composite: Synthesis and photocatalytic mechanism, *Mater. Res. Bull.* 115 (2019) 140–149.
54. Sun, Xiaofeng, et al. "Enhanced photocatalytic and photo-Fenton catalytic activity of BiFeO_3 polyhedron decorated by AuAg alloy nanoparticles." *Journal of Materials Science: Materials in Electronics* (2021):1-17.

Figures

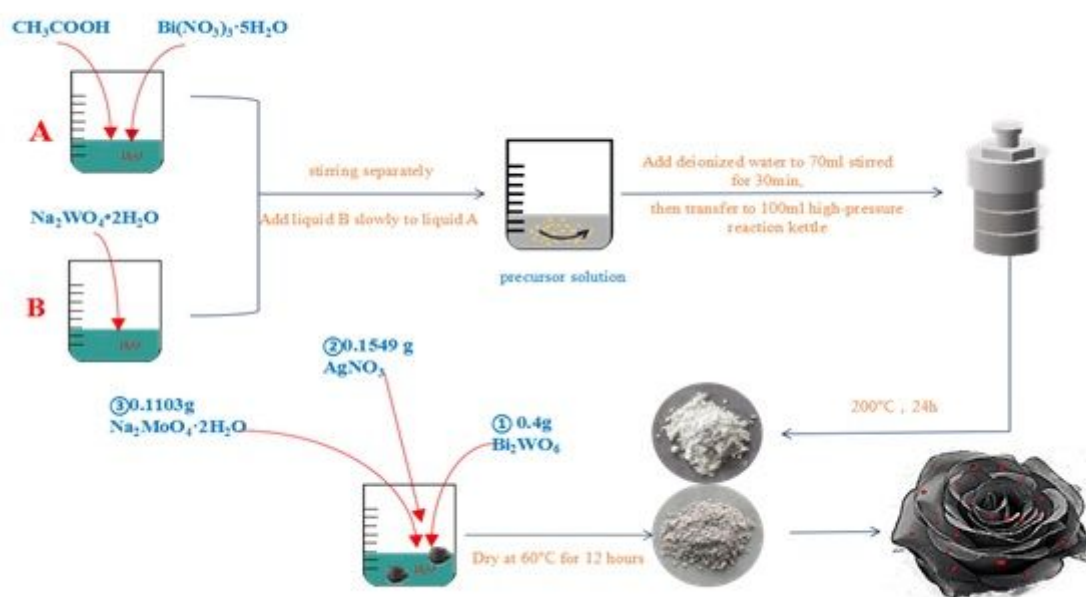


Figure 1

Schematic preparation process of 30wt%AMO/BWO composite.

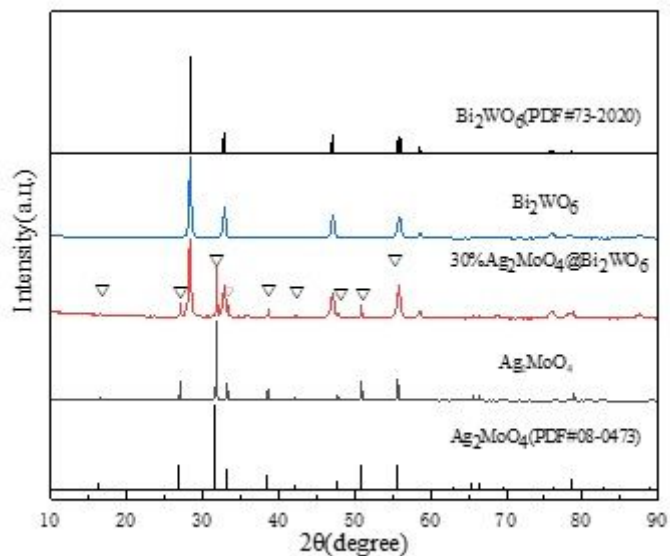


Figure 2

XRD patterns of AMO, BWO and 30wt%AMO/BWO.

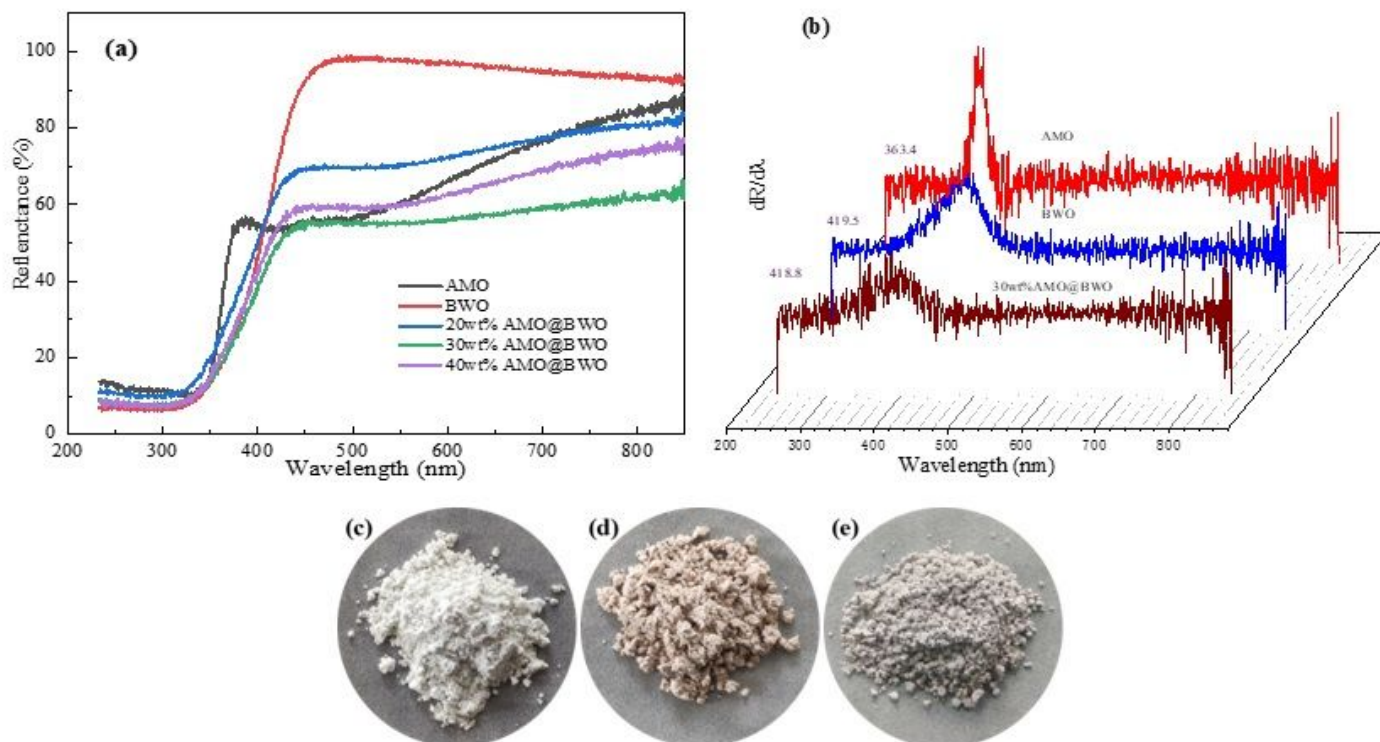


Figure 3

(a) Ultraviolet-visible DR spectra of BWO, AMO and AMO/BWO composite materials; (b) Differential curves of the ultraviolet-visible DR spectra; (c)-(e) apparent colors of BWO, AMO and 30wt%AMO/BWO, respectively.

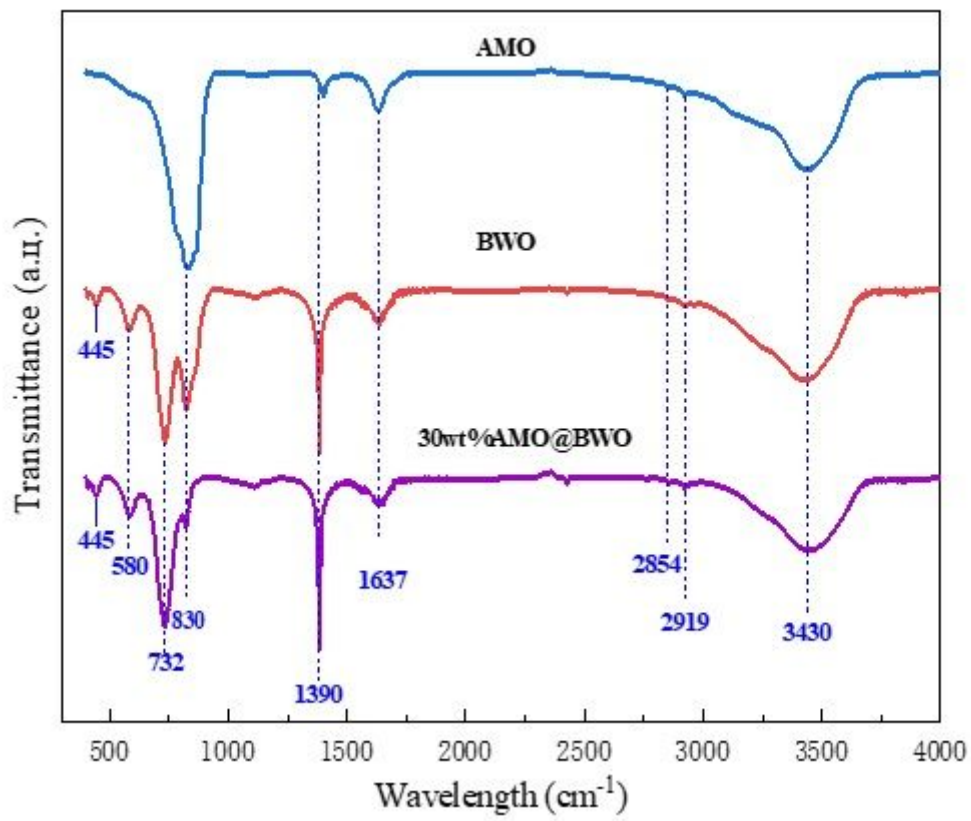


Figure 4

FTIR spectra of AMO, BWO and 30wt% AMO/BWO.

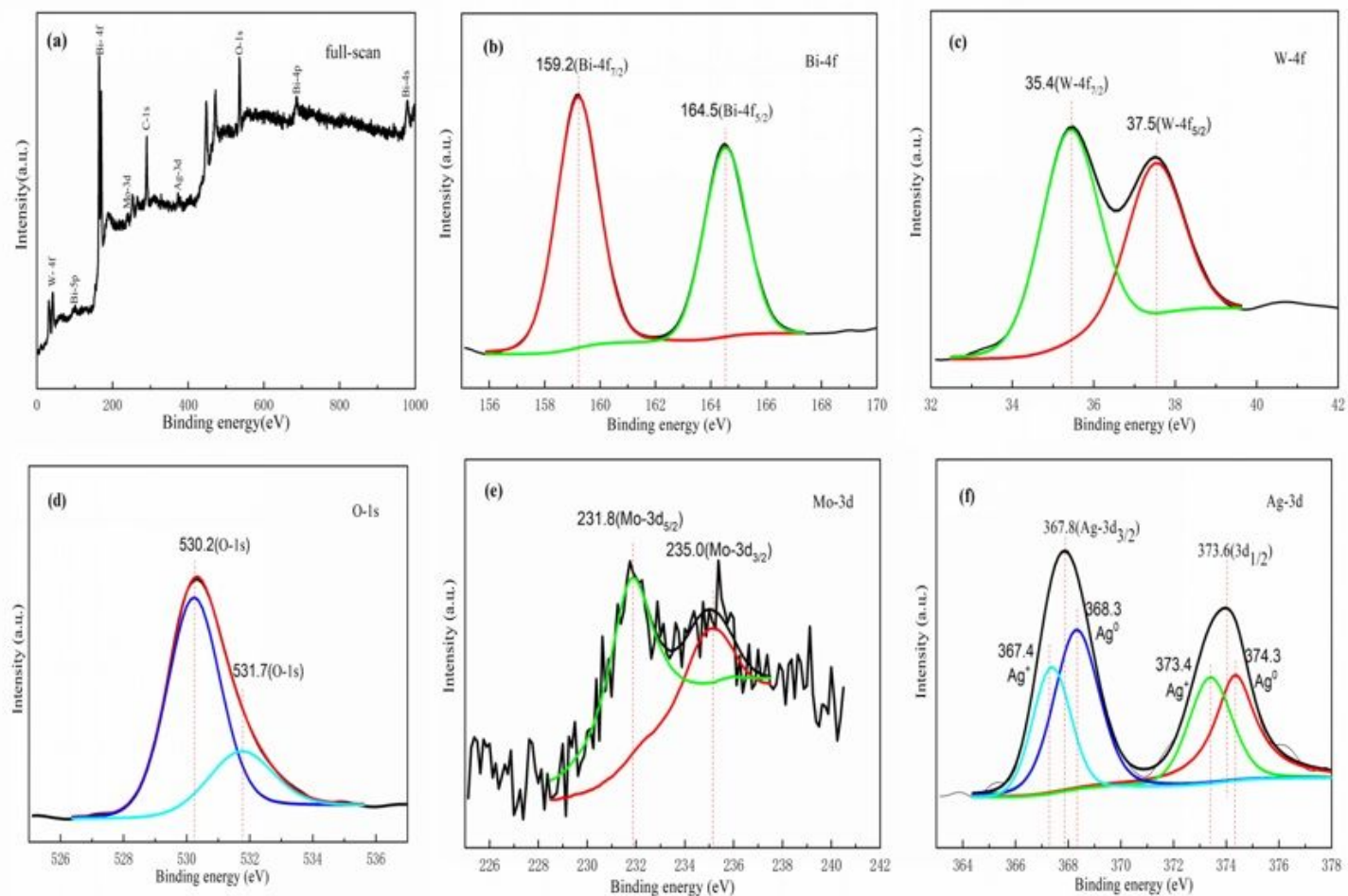


Figure 5

(a) full-scan, (b) Bi-4f, (c) W-4f, (d) O-1s, (e) Mo-3d and (f) Ag-3d core level XPS spectra of 30wt% AMO/BWO.

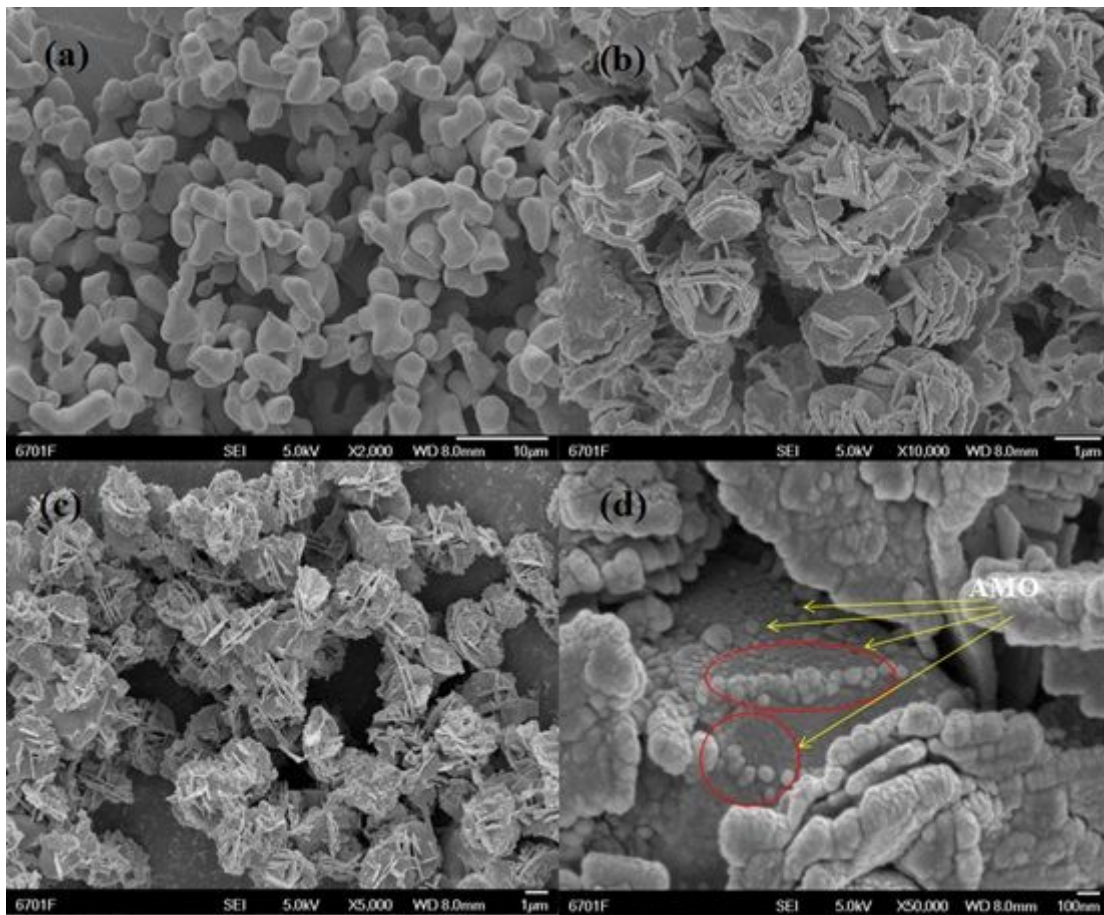


Figure 6

SEM images of (a) AMO, (b) BWO, and (c–d) 30wt% AMO/BWO.

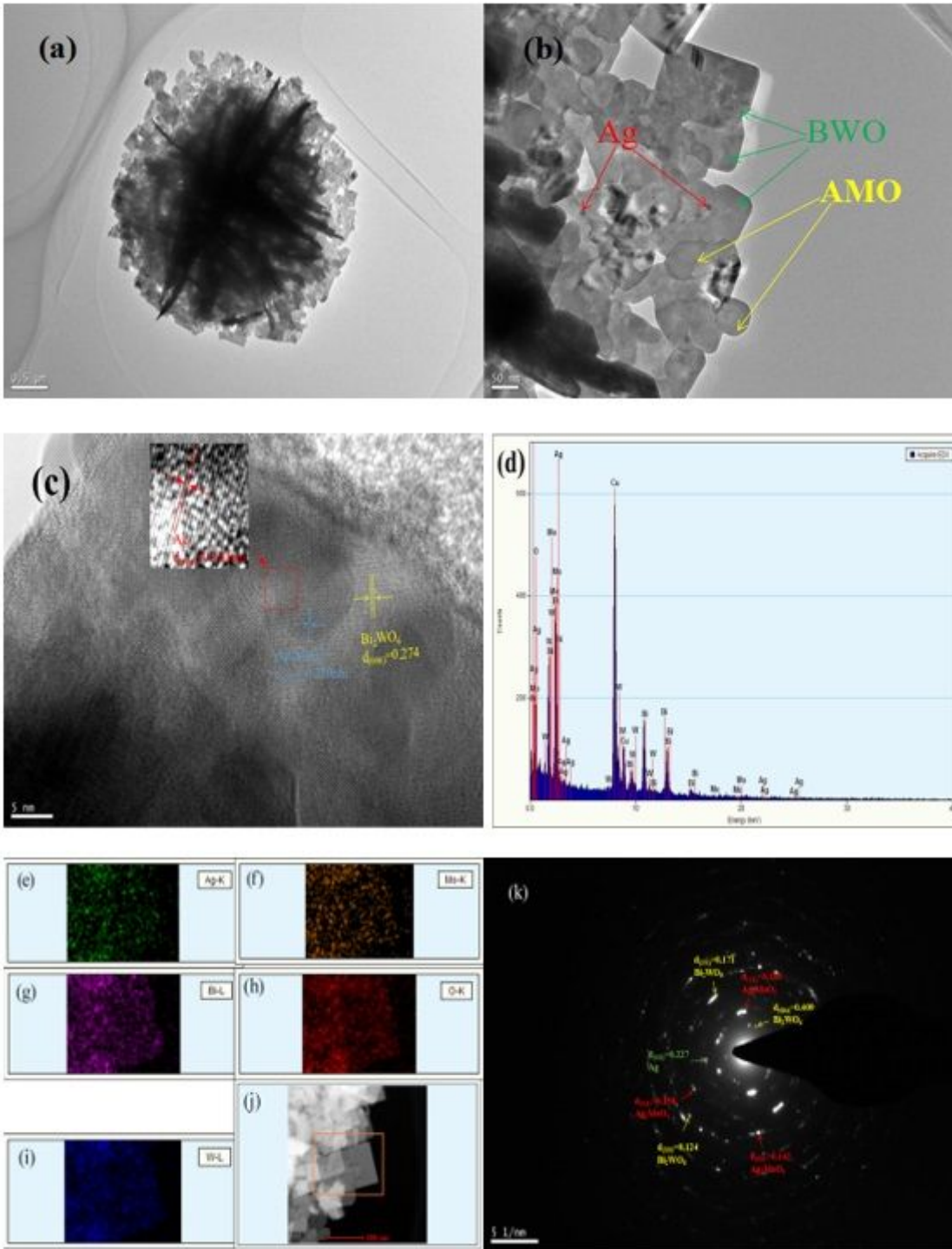


Figure 7

TEM images (a-b), HR-TEM image (c), SAED pattern (g), EDS spectrum (d), (e-i) EDS element mapping images and (j) DF-STEM image of 30wt% AMO/BWO.

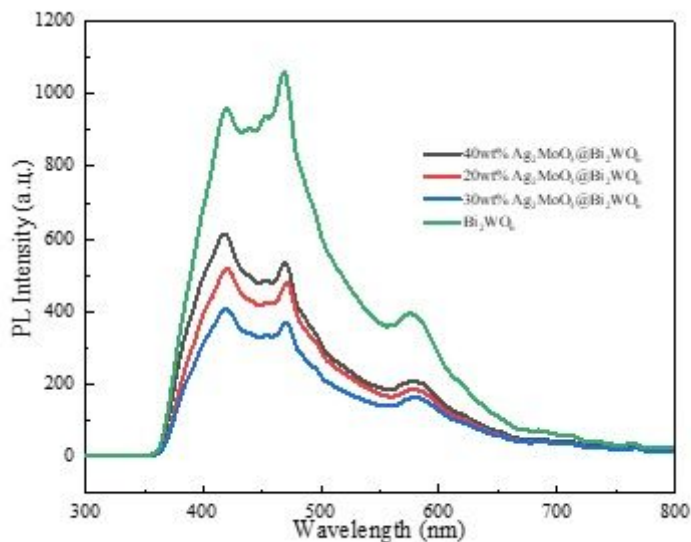


Figure 8

Photoluminescence spectra of BWO and AMO@BWO composites measured at 270nm excitation wavelength.

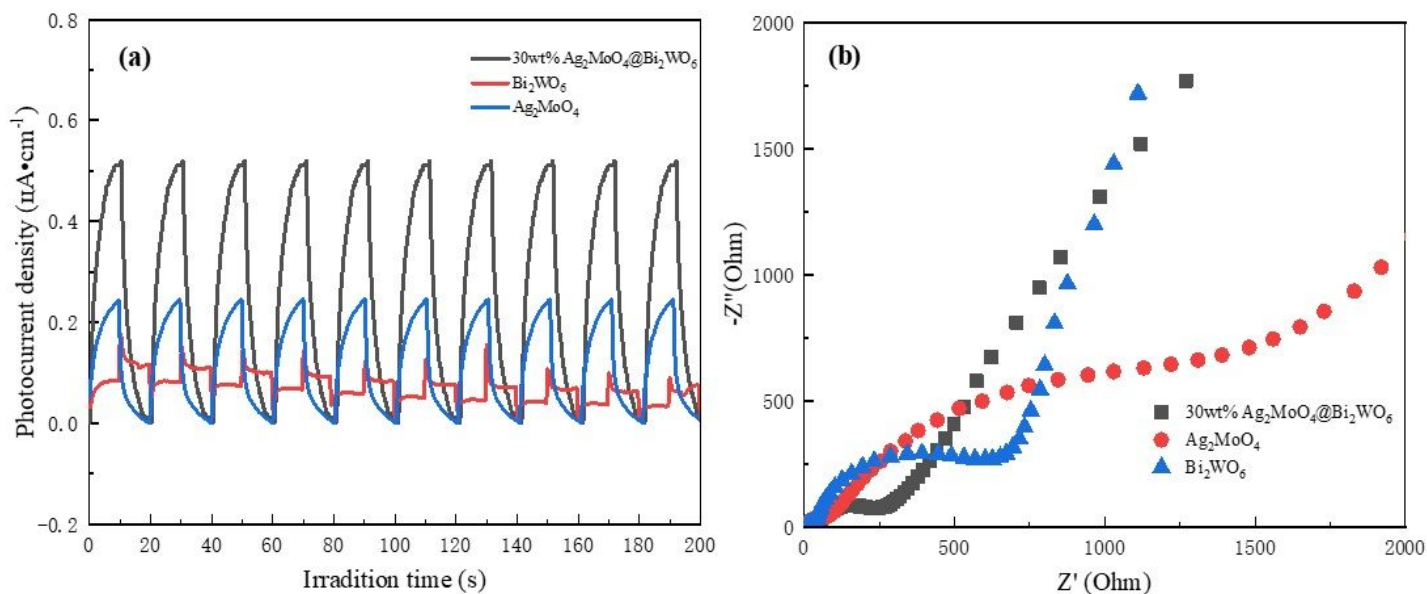


Figure 9

Photocurrent spectra (a) and EIS spectra (b) of AMO, BWO and 30%AMO@BWO.

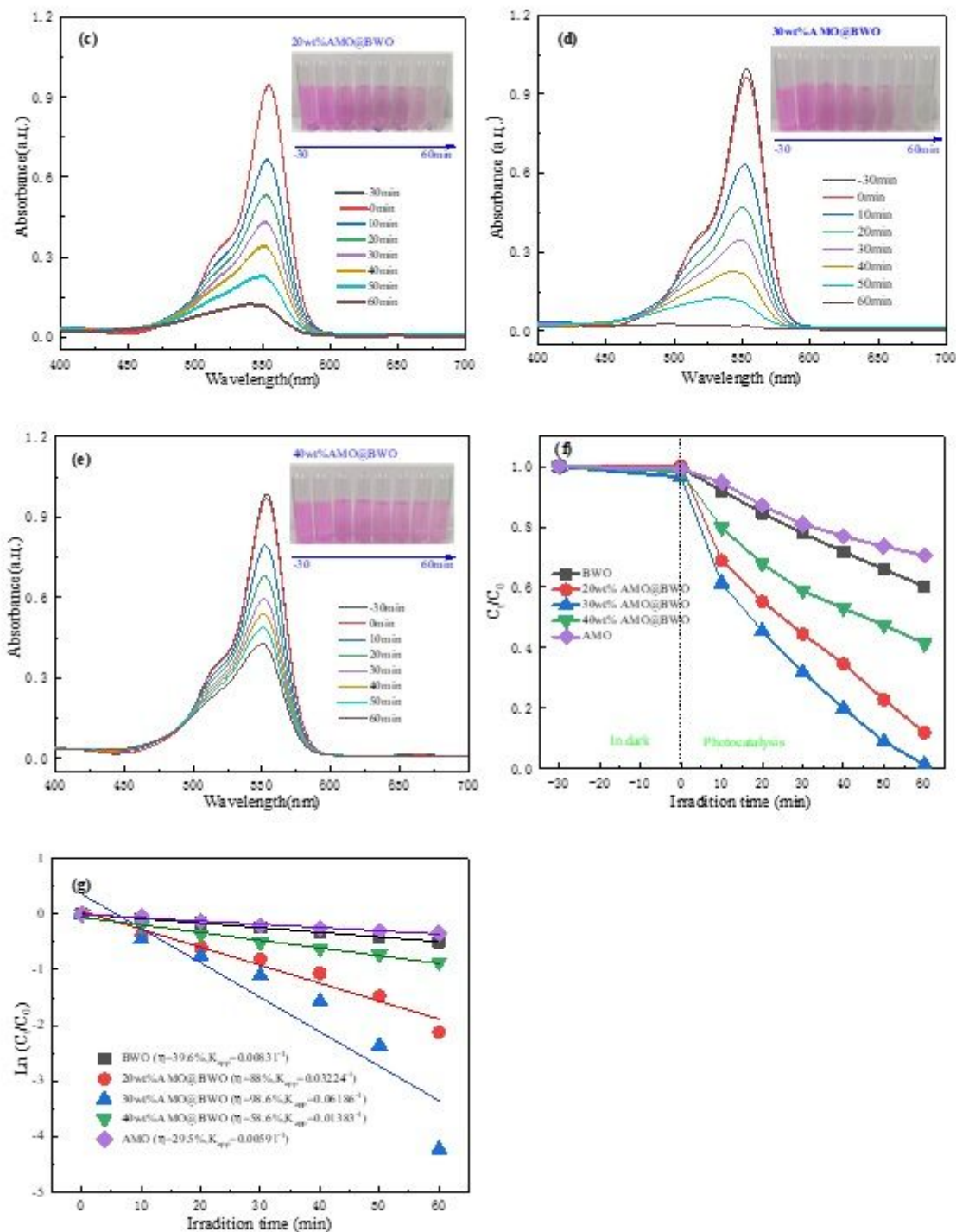


Figure 10

(a)-(e) UV-visible absorption spectra of AMO, BWO, 20wt%AMO@BWO, 30wt%AMO@BWO, 40wt%AMO@BWO, respectively; (f) and (g) Photodegradation curves and pseudo-first-order kinetic diagrams of RhB degradation over the samples.

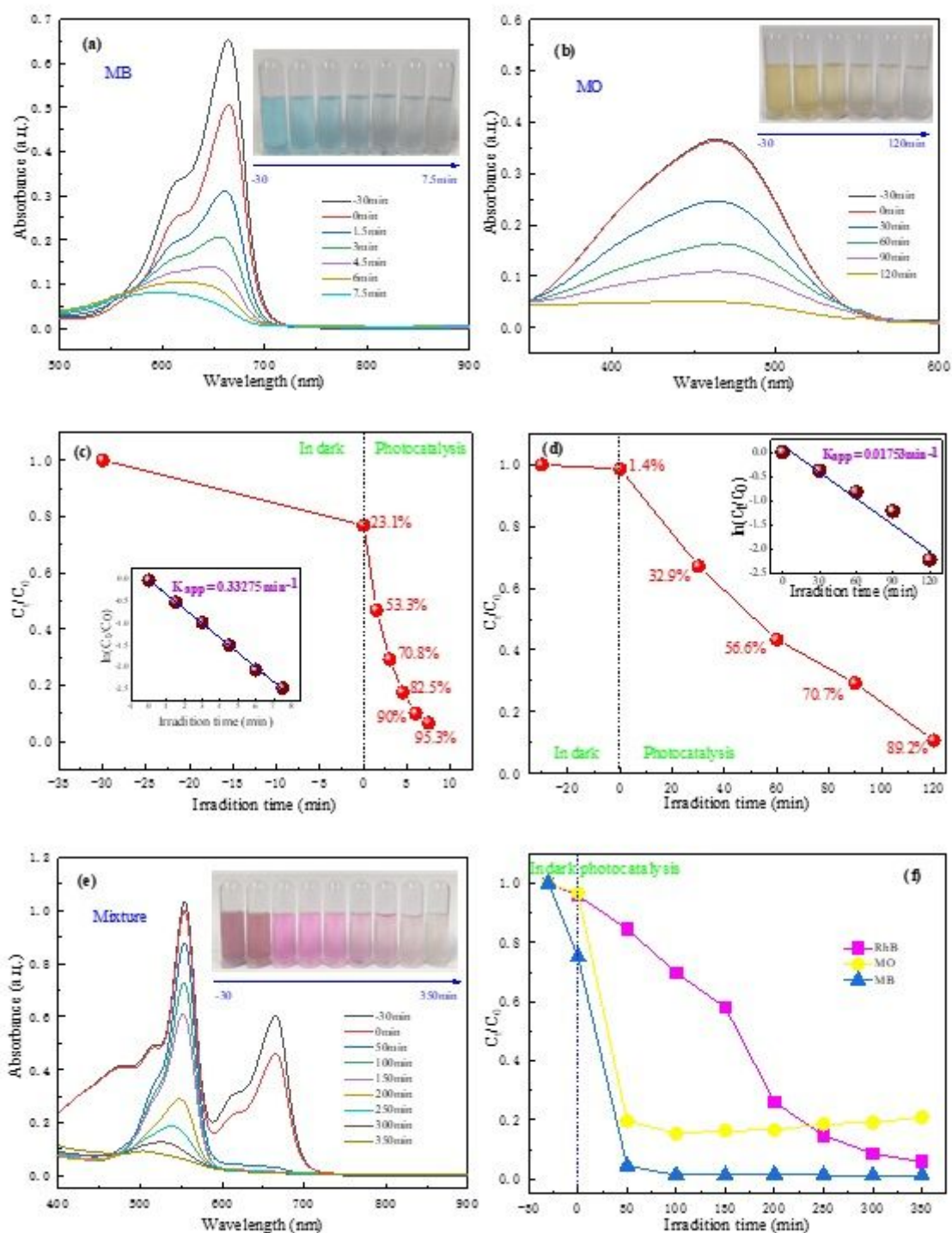


Figure 11

(a), (b) and (e) UV-Vis absorption spectra of MB, MO and RhB/MO/MB mixture solutions, respectively; (c) and (d) Photodegradation curves and corresponding pseudo-one kinetic curves of MB and MO, respectively; (f) Photodegradation curves of RhB, MO and MB in the mixture solution.

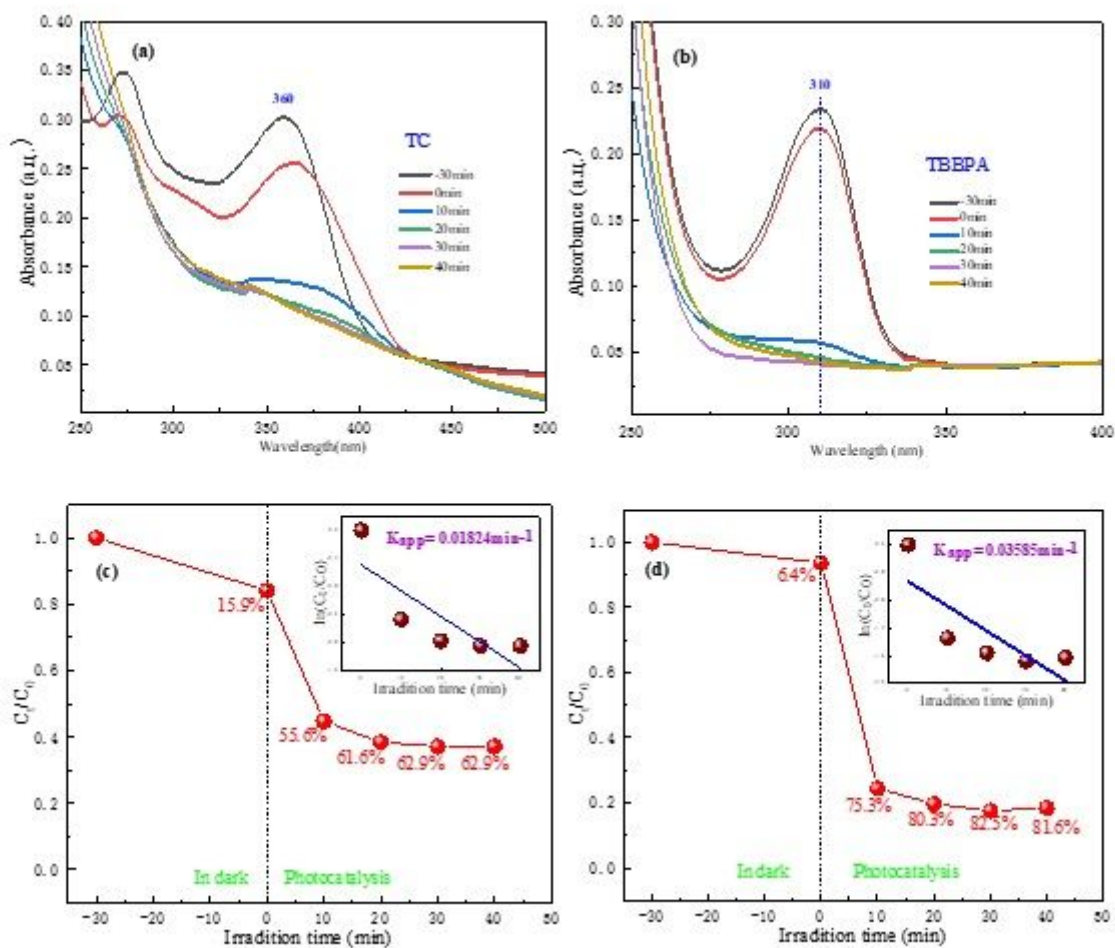


Figure 12

(a) and (b) Ultraviolet-visible absorption spectra of TC and TBBPA photodegraded by 30wt% AMO/BWO, respectively; (c) and (d) Photodegradation curves and the corresponding pseudo-one kinetic curves of TC and TBBPA degradation, respectively.

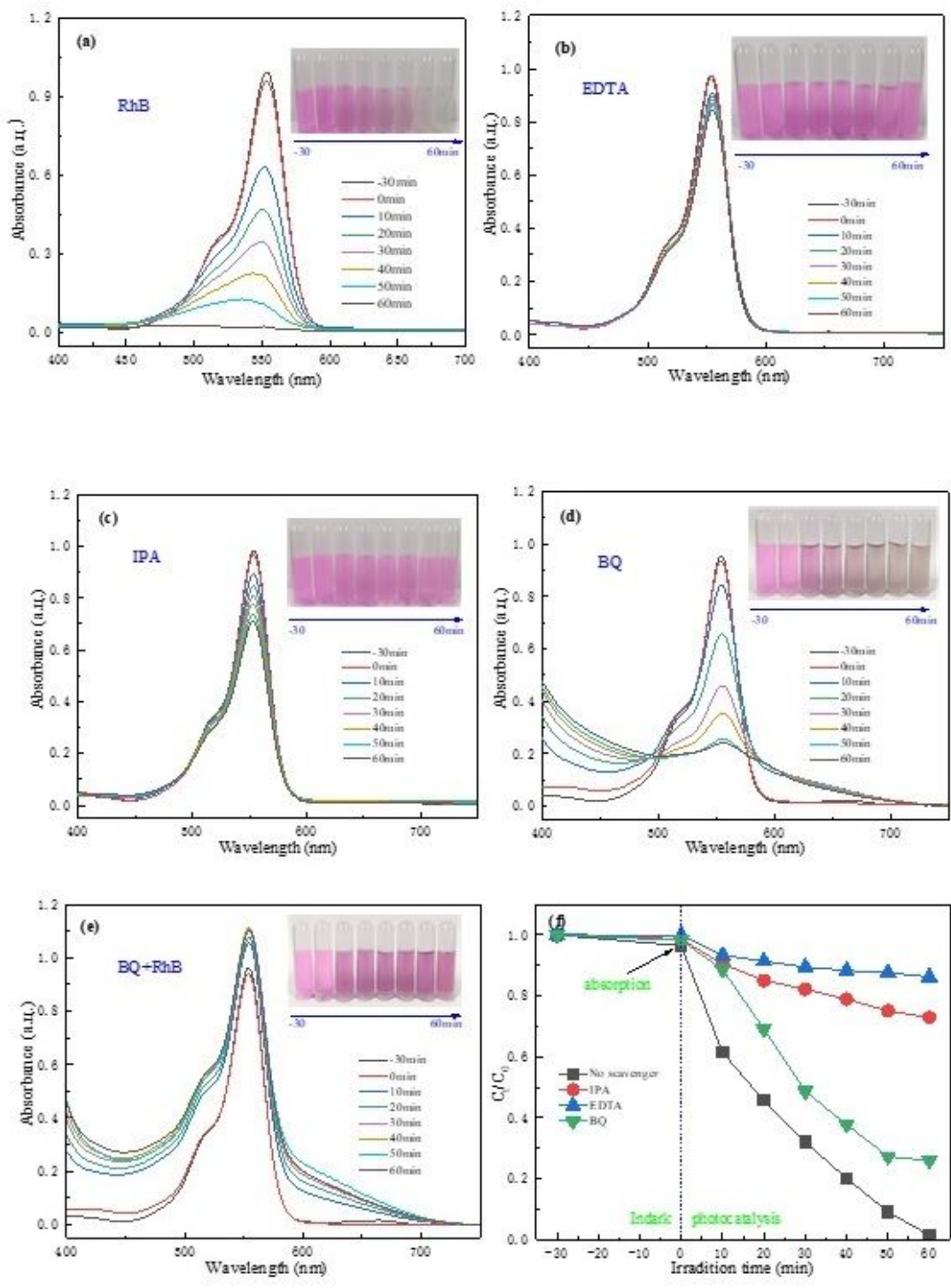


Figure 13

The photodegradation reaction species capturing experiment:(a)-(d) UV-Vis absorption spectra of RhB without adding any scavenger, and with adding EDTA, IPA and BQ, respectively; (e) UV-Vis absorption spectrum of the blank RhB+BQ solution without photocatalyst; (f) The photocatalytic degradation curves of RhB without and with adding the three scavengers.

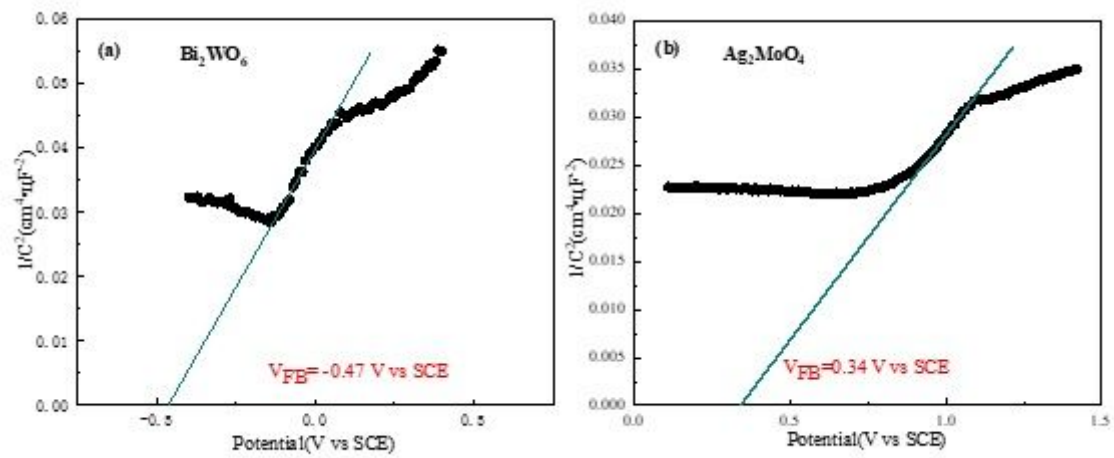


Figure 14

Mott-Schottky diagrams of (a) BWO and (b) AMO measured at 5000 Hz.

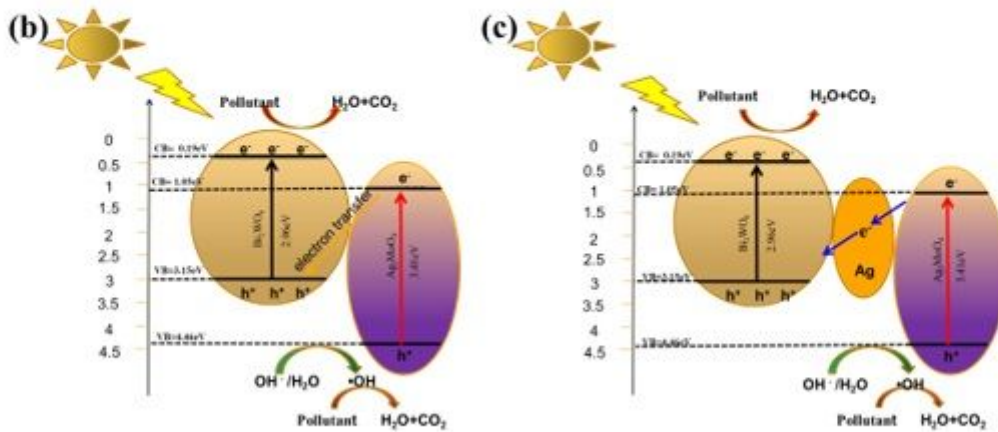
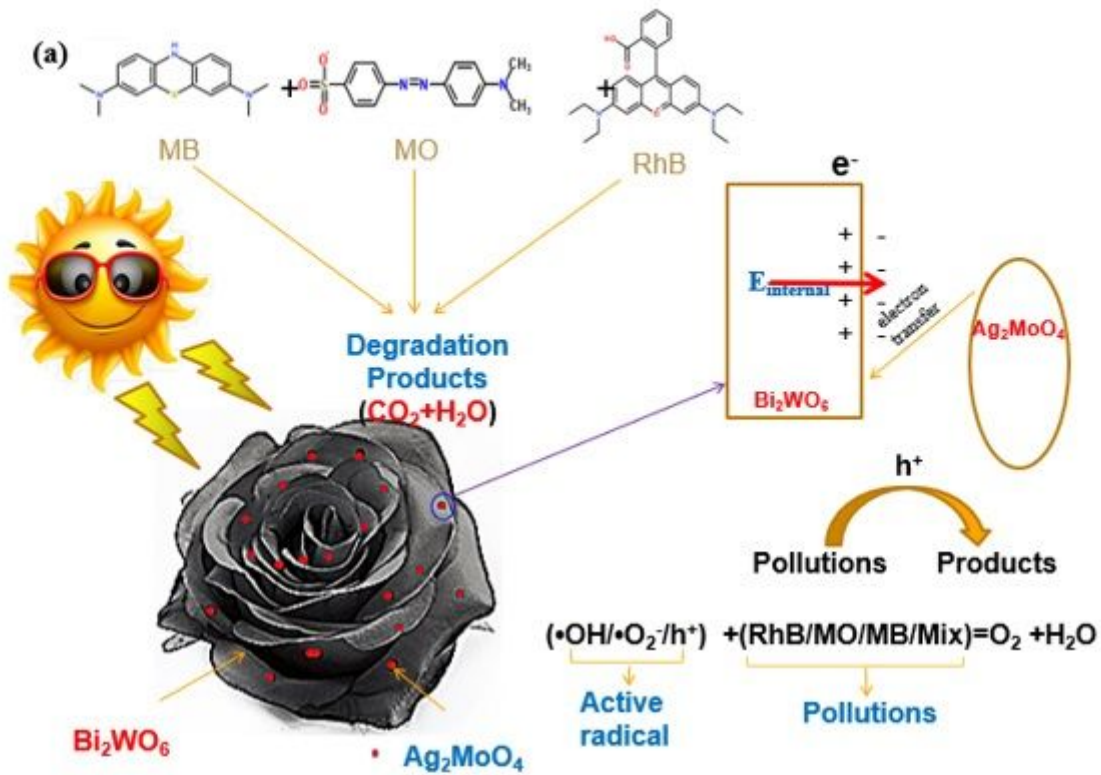


Figure 15

(a) Z-scheme heterojunctions constructed by decorating AMO particles on a rosette-like BWO hierarchical structure; (b) and (c) Z-scheme electron transfer process of AMO/BWO and AMO/Ag/BWO, respectively.